Finite Element Based Model of Fiber-optic Strain Sensor Mounted on a Semi-monocoque Structure

Jeffrey Ouellette,[*] and Alexander Chin[†]
NASA Langley Research Center, Hampton, Virginia, 23681, U.S.A.

Fiber-optic strain sensing (FOSS) provides an opportunity for additional awareness and can enable other mitigations such as flutter suppression or gust load alleviation but requires an accurate computational model as part of a design process that integrates structures and controls. A modeling approach for fiber-optic strain sensors has been developed using a shell element formulation in a detailed finite element model. The new FOSS modeling approach is designed to better scale to more complex realistic structures and fiber layouts than previous approaches. The modeling method was applied to the X-56A vehicle and results were compared to experimental static ground-test data. Additionally, the experimental sensor noise of these fiber optic sensors was assessed for the correlations in time and correlations along the fiber. The noise does show significant correlations both in time and along the fibers. These correlations of the noise should also be considered in modeling and assessing algorithms that will use FOSS.

Nomenclature

proj	Vector projection
$\hat{\mathbf{t}}_{elem}$	Direction vector defining the element $x-y$ plane
$\hat{\mathbf{t}}_{fiber}$	Orientation vector of the strain sensor
W_{bw}	Kernel function bandwidth
W_i	Weighting of each element strain contribution to the sensor output
$\hat{\mathbf{x}}_{elem}$	Element local x-coordinate
$\hat{\mathbf{y}}_{elem}$	Element local y-coordinate
$\hat{\mathbf{z}}_{elem}$	Element local z-coordinate

Symbols

δ_{ye}	Distance between the strain sensor and the element center
ϵ_i	Strain of the i-th element in the direction of the strain gauge
$\epsilon_{grating}$	Strain output for the sensor
ϵ_{xx}^{hi}	Normal strain of the i-th element in the local x-direction due to the h-th mode
ϵ_{yy}^{hi}	Normal strain of the i-th element in the local y-direction due to the h-th mode
ϵ_{xy}^{hi}	Engineering shear strain of the i-th element in the local coordinates due to the h-th mode
θ_i	Angle of the strain sensor on the i-th element

I. Introduction

There is a trend in aircraft development to create lighter and more fuel efficient structures, which is resulting in increasing flexibility and lower structural margins. The trend is especially apparent in unconventional vehicle configurations, such as high aspect ratio flying wings or next generation transport configurations. There is also the emergence of many new sensing concepts that offer great potential in the ability to improve understanding and enable control of the structure of these very light and flexible vehicles. The Helios (Aerovironment, Arlington, Virginia), shown in Fig. 1, mishap investigation showed that large deformations had an impact on the vehicle dynamics, in particular the stability of the phugoid mode [1]. Better in-flight measurement of the vehicle's structure can improve situational awareness and flight safety by enabling mitigation of these problems.

---

[*] Research Aerospace Engineer, Aeroelasticity Branch, Member AIAA.

[†] Aerospace Engineer, Structural and Thermal Systems Branch.

Fig. 1 The Helios (AeroVironment, Arlington, Virginia) unmanned aerial vehicle in flight [Source: NASA/Carla Thomas].

Historically, most work in analysis and control of an aircraft structure has made use of accelerometers [2]. However, each accelerometer requires two or more wires. The fidelity of what can be estimated in flight becomes limited by the space to accommodate these wires and the time to run them through a confined space such as a wing. Foil strain gauges are also useful for structural measurement; however, they still require a large number of wires. The required space for a large number of foil strain gauges, limits the number of gauges that can be applied to a wing. Strain gauges have typically been unable to provide measurements at enough locations on the wing for estimation of dynamic states and have therefore been limited to load estimation.

The introduction of fiber-optic sensing system (FOSS) offers a potential shift in the paradigm of structural sensing. It is possible to get thousands of strain measurements from a single fiber optic cable. There are many different approaches to fiber optic strain sensing. For the present work, a fiber-optic strain sensing method called optical frequency domain reflectometry (OFDR) [3] has been used. Fiber Bragg gratings are introduced to the fiber to reflect and refract a laser shone through the fiber. The reflections of the laser can be processed to give the elongation of the fiber, and thus the strain at the grating location. The OFDR approach has the advantage of allowing a large number of gratings and strain measurements along the wing. The large number of gratings require a trade-off in a limited sampling rate of around 40 Hz. Although a higher sampling rate would be beneficial, the sampling rate of OFDR has been sufficient for the present work. The highly distributed nature of the FOSS system offers opportunities to look at many thousands of spatially distributed measurements at a single time.

Often efforts to model FOSS have attempted to simplify the structure, such as a beam [4, 5]. These approaches are effective at modeling the overall deflections; however, it may not capture localized strains. Another method to model FOSS is to add fictitious elements to the finite element model [6]. These fictitious elements are defined by additional nodes at each of the grating locations. Assuming a fictitious beam between these additional nodes, it is straight forward to calculate the strain due to the changes in displacement between these nodes. The straight-forward approach of fictitious elements is appealing. However, the definition of these nodes requires the addition of small masses, to avoid a singular mass matrix, and the definition of splines to the existing finite element model (FEM) nodes. The method of fictitious elements does require reworking the FEM, and care must be taken to avoid changing the modal characteristics. Furthermore, the splining to the original structure has a significant and nonintuitive effect on the resulting strain outputs. The approximations of the actual structure needed to create the finite element model produce localized areas with large strain errors. If the nodes of the elements with these localized errors are splined to the fictitious elements, there can be large erroneous variations in the strain along the fiber. Also, these fictitious elements have generally been applied to straight runs of the fiber, without changes in direction that can be more useful for measuring shear strains. Suh et al. [6] suggest more complicated structures or fiber layouts will require more direct usage of the strain outputs of the finite element model.

To create a more general model that will scale to more complex configurations than the fictitious elements used by Suh et al. [4–6], a new method was developed to directly use the strain outputs from the FEM. The FEM strain outputs are processed to correct for the orientation of the fiber/grating/gauge. Because strains from multiple elements are available, a smoothing between elements is applied to adjust for any local errors. The method has been applied to the X-56A (Lockheed Martin, Bethesda Maryland) Multi-Utility Technology Testbed (MUTT), and comparisons of the strain are made between the FEM-based model and static loading ground tests.

II. Modeling of Strain Measurements

A single fiber optic cable is capable of providing on the order of thousands of strain measurements. This is a significant reduction in weight simply by reducing the cabling that would be required for a more traditional sensor such as an accelerometer. Furthermore, the strain is algebraically related to the generalized modal coordinates, rather then a differential relationship like accelerometers. Unlike other sensors, e.g., accelerometers and gyros, which can be taken directly from mode shapes, the derivation of a strain sensor requires the curvature (or similar geometric details) of the deformed shape.

For the current work, the focus was on a fiber optic sensor that had been mounted on the skin of the wing. The fiber was mounted close to where the skin was attached to the spar to maximize the strain transfer. The wing skin represents a convenient location for mounting, and shell elements will be the most representative element for mounting the fiber on the skin. The strains are associated with elements rather then nodes. Looking at the center of the element avoids discontinuities in the strains at the nodes, between the elements, which are an artifact of the finite element modeling. These discontinuities can be caused by the shape functions in some finite elements or by changes in material properties between elements. The finite element model was setup to output the normal strain in the element x-direction and y-direction, ϵ_{xx}^{hi} and ϵ_{yy}^{hi}, as well as the engineering shear strain, ϵ_{xy}^{hi}, (twice the true shear strain) for each of the shell elements in the vicinity of the fiber optic cable. The FEM was setup to give the strains at the center of each element.

The strain will differ slightly between these upper and lower surfaces of a shell element due to the thickness of the element. The element coordinate system is shown in Fig. 2. When the element is defined, the ordering of the grid points stipulates which is the upper and lower surface of the element.

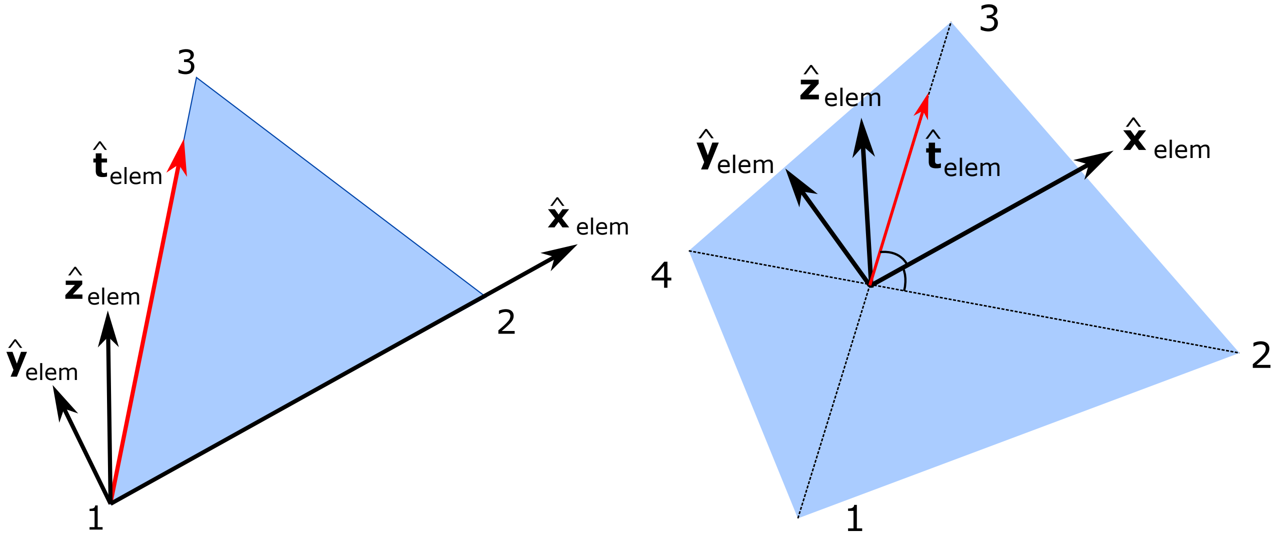

a) Triangular element coordinate system. **b) Quadrilateral element coordinate system.**

Fig. 2 Element coordinate system definitions.

To ensure the correct strain is used in the FEM-based model, care must be taken to ensure that the strain from the outer surface, where the fiber is mounted, is selected. This process was automated by grouping elements into the upper and lower surface of the wing, and then comparing the element normal vector to the global z-direction.

A. Rotation of Strains

To calculate the orientation of the strain measured by the grating, a tangential vector is defined along the fiber, $\hat{\mathbf{t}}_{fiber}$, for each grating. The fiber tangential vector is projected [7] onto the elements, Eq (1).

$$\text{proj}_{elem}\hat{\mathbf{t}}^{i}_{fiber} = \hat{\mathbf{t}}_{fiber} - \frac{\hat{\mathbf{t}}_{fiber} \cdot \hat{\mathbf{z}}_{elem}}{\|\hat{\mathbf{z}}_{elem}\|^2}\hat{\mathbf{z}}_{elem} \tag{1}$$

The angle of the grating, θ_i, is defined as the angle between the fiber's projected orientation and the element's x-coordinate. The angle is calculated using the dot product, Eq (2).

$$\cos\theta_i = \frac{\hat{\mathbf{x}}_{elem} \cdot \text{proj}_{elem}\hat{\mathbf{t}}_{fiber}}{\left\|\text{proj}_{elem}\hat{\mathbf{t}}_{fiber}\right\| \, \|\hat{\mathbf{x}}_{elem}\|} \tag{2}$$

For plate elements, the strains represent plane strain. Once the angle of the gauge is known, the strain tensor is then a typical rotation of plane strain [8], Eq. (3).

$$\epsilon_i = \epsilon^{hi}_{xx}\cos^2\theta_i + \epsilon^{hi}_{yy}\sin^2\theta_i + \epsilon^{hi}_{xy}\sin\theta_i\cos\theta_i \tag{3}$$

This section has described the general approach for calculating the strain output of each grating as a function of the modal coordinates. The formulation of the FEM-based model presented here is shown in a form to improve readability. To maximize computational efficiency, when coding these computational models these calculations can also be implemented in an equivalent vectorized approach with elemental operations and Kronecker delta products.

B. Smoothing/Interpolating

The FEM was setup to provide the strain at the center of an element. However, in general the elements are not coincident with the gratings in the fiber. The most obvious approach to interpolating these strains to the gratings, is to select the element center closest to the grating, i.e., nearest neighbor interpolation, Fig. 3a.

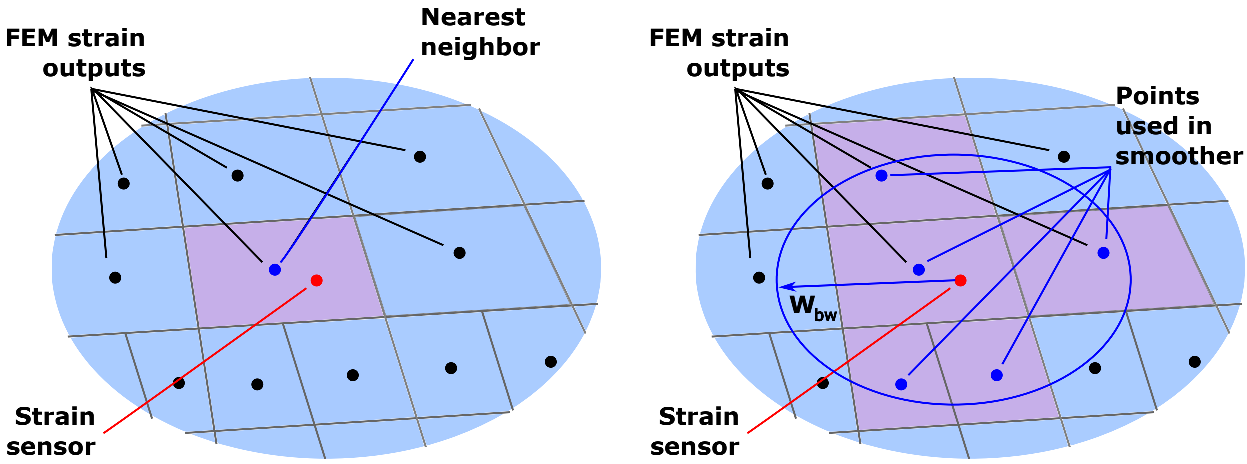

a) Nearest neighbor interpolation for strain output. **b) Kernel smoothing for strain output.**

Fig. 3 Interpolation and smoothing methods for strain sensor output.

The nearest neighbor approach worked reasonably well. However, with a FEM, some elements can have significantly different strain then their neighbors as shown in Fig. 4. As a result, the FEM-based model of the gratings showed much larger variations along the fiber than was observed in testing.

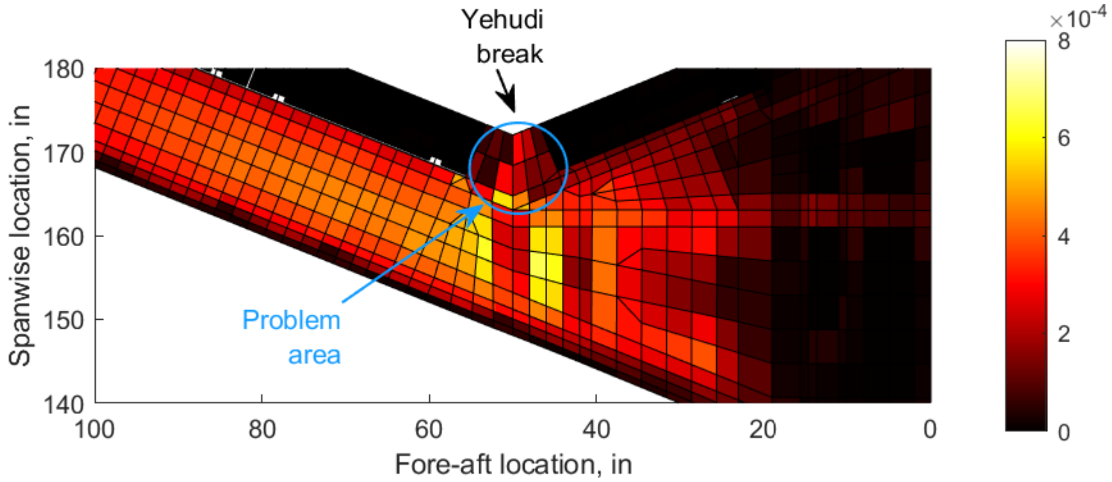

Fig. 4 Variation in strain between elements showing elements with higher strain for first wing bending mode.

In general, the aeroelastic FEM for a complete aircraft is designed to represent the overall dynamics and deformations. The FEM is not optimized to give accurate representation of the localized strains. The idea of the idealization of the structure is formalized by St. Venant's principle [8]. By St. Venant's principle, when sufficiently far enough away from an applied load or discontinuities in boundary conditions, such as where the skin and ribs are connected, the error in the strain is small for a statically equivalent loading. However, the strain gauges can be located directly on these discontinuities, which makes it difficult or impossible to capture measured strain in a FEM of a complete vehicle used in aeroelastic analysis. For example, if a grating is directly on a rib, the area will be stiffer, and the strain will be lower. The idealization of the aircraft's structure to produce a FEM of a complete aircraft often do not accurately model these localized effects. These localized errors cause many of the elements with much larger strains at the aft of the wing in Fig. 4.

To reduce the sensitivity of the FEM-based model, $\epsilon_{grating}$, to elements with erroneously large strains, the interpolation method was replaced with a smoothing method. In interpolation, if the grating were located at the element center, the grating would be exactly equal to the element solution. In contrast, with the smoothing, all the neighboring elements still have some effect. A kernel smoothing approach, Fig. 3b, is used. The kernel smoother, Eq. (4), uses a weighting, W_i, based on the distance from the element center to the grating, δ_{ye}.

$$\epsilon_{grating} = \frac{\sum_i^k \epsilon_i W_i}{\sum_i^k W_i} \tag{4}$$

There are many different choices for kernel functions. However, for the current work the tricube kernel, Eq. 5, was selected. The tricube kernel will emphasize the elements that are closest, and therefore most relevant, to the grating. The tricube kernel is also beneficial because it has a finite bandwidth. The finite bandwidth, W_{bw}, means that elements outside this distance have zero effect on the FEM-based model. Because the kernel goes to zero, the matrix used in the calculations is sparse. The sparse matrix is significantly faster to calculate and requires less computer memory. For the current work, the bandwidth was selected to be roughly the typical element size, $W_{bw} = 4$ inches. This means that the grating's sensed strain will be a function of only the elements in the immediate neighborhood of the grating.

$$W_i = \begin{cases} \left(1 - \left(\frac{\delta_{ye}}{W_{bw}}\right)^3\right)^3 & \delta_{ye} \le W_{bw} \\ 0 & \text{otherwise} \end{cases} \tag{5}$$

III. Calibration of the FEM-based model

The FEM has generally done a good job predicting the strains, but simplifications and assumptions in the FEM will produce errors in the strains. One of the primary examples of these errors is because the FEM approximates the curvature of the wing as depicted in Fig. 5. Because the strain is directly proportional to the offset from the neutral axis, the approximations of the curvature in the FEM cause a scaling error in the strain outputs. These errors are most pronounced when the fiber is mounted close to the leading edge of the wing.

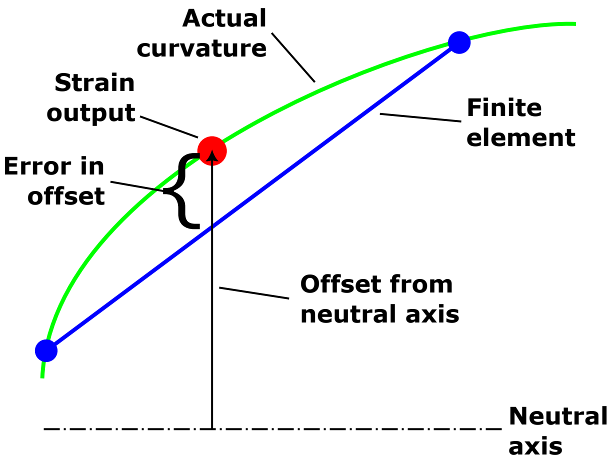

Fig. 5 Strain errors due to curvature.

The errors due to the curvature are generally the largest, but strain measurements do often have other scaling errors such as the quality of the bond. There are also errors in the strain measurements due to localized effects, as was shown in Fig. 4. Attempting to correct the FEM-based model to match these localized effects could increase the errors in the FEM-based model. Also, the correction factors need to consider the noise in the measured data to avoid over fitting the corrections.

To reduce the occurrence of these errors, a calibration correction was derived. Experimental static loading ground-test data was used for calculating the correction factors. A separate correction for each strain output is calculated to exactly match the measured strain data. Next a smoothing was performed along the 788 strain outputs on each fiber. The smoothing helps to remove the local errors and reduce the noise effects. The smoothing was done in four steps.

1) Five-point median smoothing
2) Any negative corrections are set to one
3) 51-point median smoothing
4) 101-point moving average

The n-point median smoothing is very similar to a moving average. Like the moving average, a window of n-points is examined. Instead of averaging the points, the median, or middle value, is used. The median smoothing is a nonlinear operation but is conceptually quite simple to implement. It has the advantage of being much less sensitive to outliers then linear smoothing methods like a moving average. The five-point median smoothing does a good job of removing any correction factors due to very localized effects.

The second step removes any points where the correction factor does not have physical meaning. There were some points were there was effectively no strain, e.g., the wing tips. In this case there is insufficient information to determine a correction factor, so it was just assumed to be one. These regions were less localized, so it was impractical to remove them with the smoother.

A second pass of the median smoother was used with a larger window to help further remove any localized effects. The nonlinear behavior of the median smoothing causes a stepping behavior in the smoothed estimates. To remove the stepping, a final moving average was applied to the corrections.

IV. X-56A Results

A. Description of Experiment

The X-56A MUTT, shown in Fig. 6, was developed specifically to study active control of the structure of an aircraft and suppression of body freedom flutter [9]. The wings of the aircraft are interchangeable to provide the ability to explore the characteristics of an aircraft with a relatively stiff structure or a flexible aircraft with unstable flutter modes. Unlike most production aircraft today, the X-56A MUTT has structural dynamics that are catastrophically coupled with the flight dynamics; with the flexible wings, the coupling is strong enough to destabilize the aircraft dynamics.

Fig. 6 The X-56A MUTT in flight [Source: NASA/Jim Ross].

The X-56A was selected as the primary example for study and has a wingspan of 28 ft. The X-56A had a realistic semi-monocoque structure with spars, ribs, and skin. The realistic semi-monocoque structure is important for assessing structural sensing technologies like FOSS. The more representative structure of X-56A allows examination of the localized strain effects that were shown in Fig. 4.

A detailed FEM of the X-56A has been developed using NASTRAN™ (MSC.Software Corporation, Santa Ana, California) and is shown in Fig. 7 and the layout of the fiber-optic sensing is shown in Fig. 8.

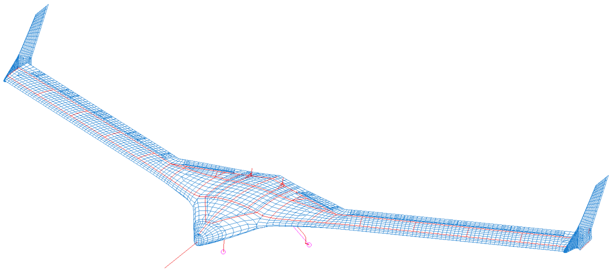

Fig. 7 The X-56A FEM model.

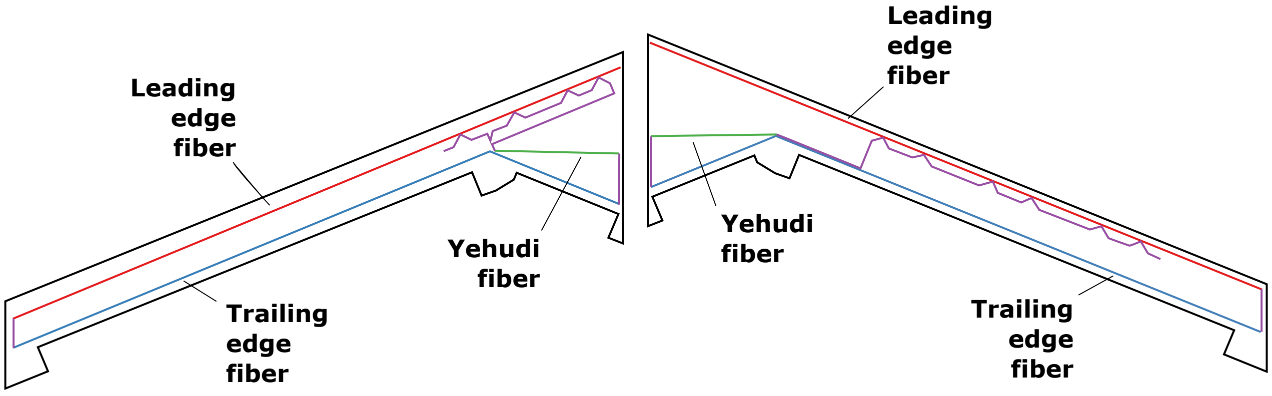

a) Upper surface. **b) Lower surface.**

Fig. 8 X-56A left wing fiber-optic layout in blue.

The zig-zag patterns were intended to better capture torsional strain. However, due to complexities in determining the true location of the gratings on the actual wing and a poor signal to noise, these portions of the fiber have not been used in the current analysis. The grating locations can be slightly different between the left and right wings. However, this effect was neglected, and the fiber layout was assumed to be symmetric from left to right. The upper and lower surfaces are very similar in layout, but there are slight differences in where the gratings end up being located due to a need to accommodate the actuator access panels on the lower surface. The fiber arrangement provided a total of 936 strain measurements at a sample rate of 40.711 Hz. Typical of the OFDR FOSS, there is a large number of strain measurements, but a relatively low sampling rate.

For X-56A static loading ground tests, the wings were mounted on a hardback in the NASA Armstrong Flight Loads Lab [10], Fig. 9. By rotating the wing and applying sandbags, a total of 14 cases shown in Table 1 were tested. These tests were performed primarily for calibrating the traditional foil gauges and validating the wing's structural strength. However, the FOSS system was also run, and the variety of load conditions do provide a good sampling for assessing the effectiveness of the strain measurements.

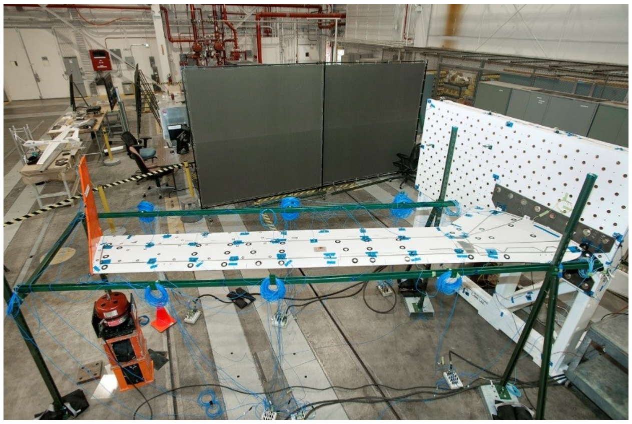

Fig. 9 X-56A flex wing static loading ground tests [Source: NASA].

Table 1 X-56A static loading ground test cases.

Case Number	Up/Down	Purpose	Total Shot Bags
1	Down	Calibration 1	15
2	Down	Calibration 2	10
3	Down	Calibration 3	8
4	Down	Calibration 4	10
5	Down	Calibration 5	15
6	Down	Calibration 6	17
7	Down	Proof	39
8	Up	Calibration 1	21
8	Up	Calibration 2	16
10	Up	Calibration 3	11
11	Up	Calibration 4	24
12	Up	Calibration 5	32
13	Up	Calibration 6	27
14	Up	Proof	57

The static loading ground tests were static loading, so they enable validation of the stiffness and strain relationships in isolation without having to consider any potential errors in the mass distribution. Half of the cases were up bending, as in flight, and half were down. There was one proof load case in each direction. The other cases were intended for calibration of the traditional foil gauges to get a measure of wing root bending. The loads were applied by putting 5 lb bags of lead shot onto the wing. The total shot bags are shown to give a reference of how much weight was on the wing for each case. The location of the bags was changed between cases to produce different torsional and bending cases that better cover the load envelope.

The static loading ground tests from the X-56A has been used for validating the implementation of the FEM-based modeling approach. The goal of this analysis is to demonstrate the validity of the proposed FEM-based modeling approach and to demonstrate the accuracy of the FEM to estimate the strains of the realistic vehicle. For each load case, a total of 512 samples, ~12.6 sec, of data is used to calculate the average displacements, the average strains, and statistics of the noise.

B. Validation of Loading and Static Deflections

Before looking at the strain outputs, the wing deflections are examined to validate the application of the load cases and FEM stiffness. The wing tip deflections for all of the load cases are summarized in Fig. 10. The estimated deflections from the FEM are compared against the experimental FOSS estimates. The FOSS estimates are using a beam model and integrated along the span.

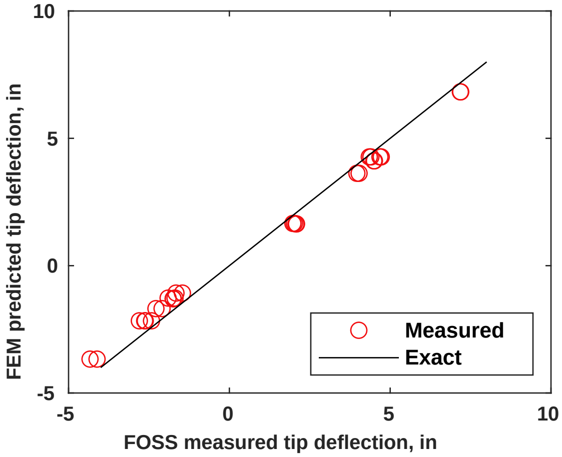

Fig. 10 Tip deflections from X-56A static loading ground tests.

The FEM displacements follow the FOSS estimate trends well. However, there is a consistent bias on all of the cases. The magnitude of the FOSS is consistently smaller than the FEM estimates. The bias could be explained by the calibration of the FOSS. If there was a bias on the strains, this would produce the observed behavior.

The spanwise deflections for 2 different load cases are shown in Fig. 11. These cases were selected to show a low magnitude case and a proof case. Although the magnitude of the deflections is small, earlier testing of the composite material of the wings show that there were material nonlinearities present for the strains at the heavier load cases, such as the proof loading. These material nonlinearities are likely to reduce the accuracy of the solution. The adjusted FOSS deflections were corrected to remove the bias in the tip deflections due to gravity loading that was observed in Fig. 10.

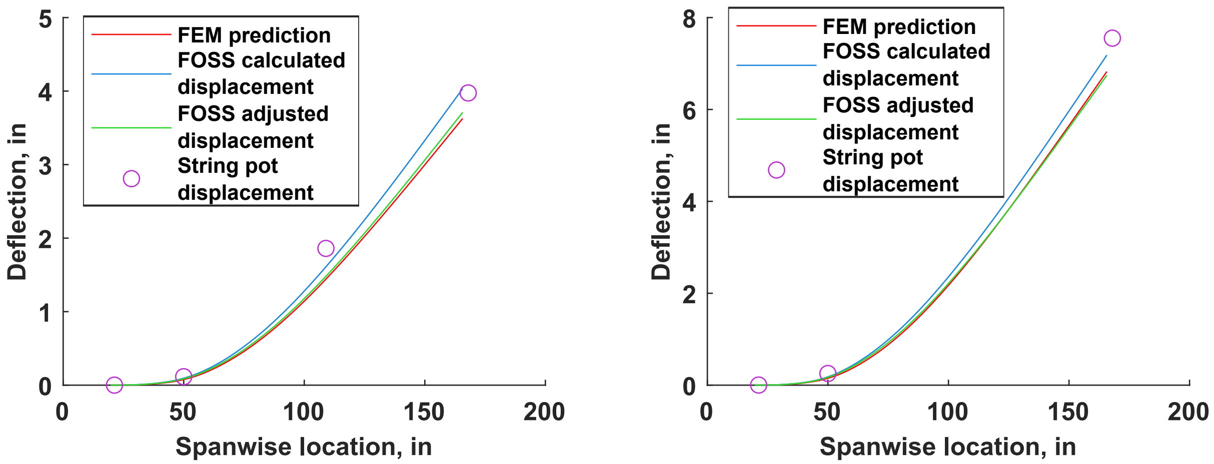

a) Left wing, up bending, load case 12.

b) Right wing, up bending, proof case.

Fig. 11 Spanwise deflections.

When the bias in the FOSS data is corrected, the FOSS and the FEM estimates match very well across the span. Neither estimate matches well to the string pot. It is expected that the string pot should be the most accurate solution, although it only provides measurements at 3 to 4 points along the span. However, the middle string pots do not match well to the FOSS or FEM deflections. During testing, it was observed that a string pot attached to the wing root was supposed to be at a fixed location, but it had moved. The string pot which moved was not included, but the remaining string pots could have had similar, but less obvious errors. Because the string pot data is suspect, it is unclear if the problem is the string pot measurements or the FEM displacements.

C. Examination of Correction Factors

Experiences with these ground tests showed problems in the dynamic strain measurements. To address these problems, the internal processing of the FOSS data was changed between these ground tests and the flight tests. The fiber location was identical, but there were additional gratings that were output for the static load testing. Because the primary interest of this work is to utilize the flight-test data to estimate the generalized modal coordinates [11] or the shape, the FEM-based model of the FOSS used the flight grating locations. If you try to interpolate the static loading ground-tests data to the location of the flight-test grating, you will be interpolating the measurement noise as well. The effect of the noise on the interpolation is difficult to predict. However, the FEM-based model has no measurement noise, so it was decided to interpolate the FEM-based model. While less direct, this approach avoids the non-deterministic effect of measurement noise on the interpolation. A simple one-dimensional interpolation was done along the fiber to translate the strains from the current FEM-based model to the locations from the static loading ground tests. The correction factor was then calculated for each of the gratings in the static loading ground tests. Once the correction factors are smoothed to reduce the measurement noise, a one-dimensional interpolation was then used to interpolate these static loading ground tests correction factors back to the grating locations in the FEM-based model. The aggressive smoothing applied to the correction factors minimizes the effect of noise on this interpolation.

To give a general idea of the magnitude of the corrections used and how they would vary between the different loading cases, the correction factors used for each FOSS gauge are shown in Fig. 12. These corrections include all of the gratings across all four fibers on the wings. All of the scaling corrections are close to one, and the larges correction used is less then two. The individual corrections show that there is some variation, going from 0.5–3, between the different load cases in Table 1. However, despite some load cases giving large corrections, the majority of the load cases give corrections that are close the to the final scaling factors that were used to correct the FEM-based FOSS model.

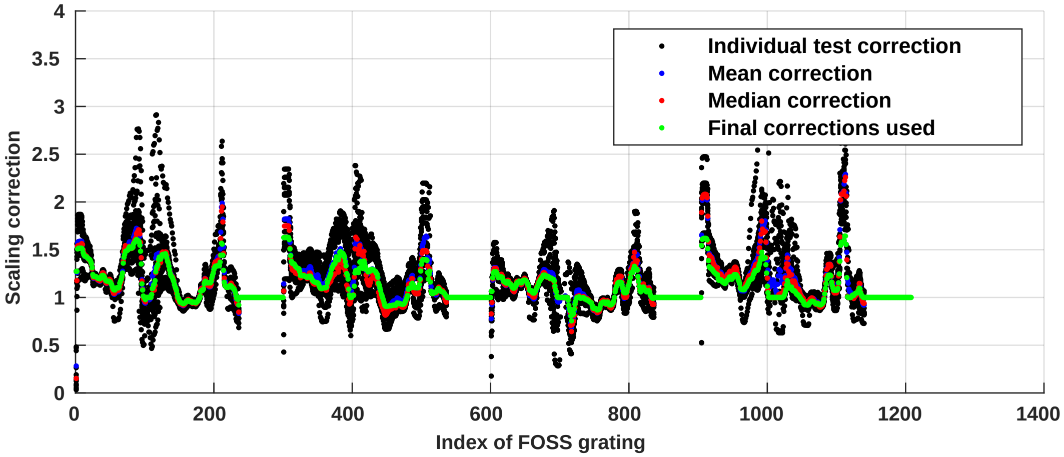

Fig. 12 Comparing correction scale factor for FOSS gratings on all four fibers for the individual load conditions.

D. Validation of FEM-based model

The strain outputs from FEM-based FOSS model and the static loading ground tests cases match extremely well for the leading edge gratings shown in Fig. 13. There is one grating for loading case 12 that shows much lower strain then the other gratings. This appears to be an anomaly of the test, since none of the other gratings show this. Additionally, the proof case does not show this outlier.

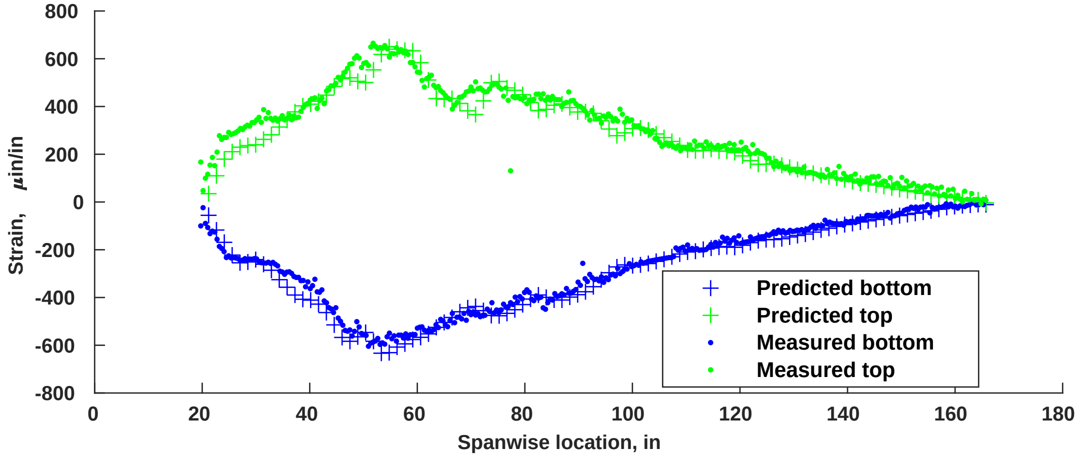

a) Left wing, up bending, load case 12.

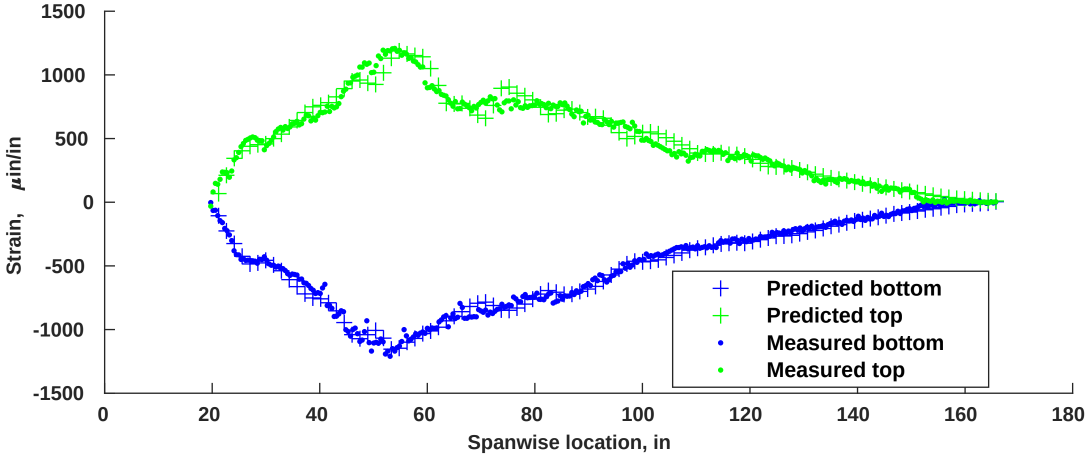

b) Right wing, up bending, proof case.

Fig. 13 Strain on leading edge fiber measured on X-56A wing during static loading and from FEM-based FOSS model.

The trailing edge gratings are shown in Fig. 14. Overall, the trailing edge FOSS FEM-based model gratings match well to the static load case data. However, the strain from FEM-based model for the bottom fiber does show a appreciably less strain at the root, as noted in Fig. 14. As shown in Fig. 4, there is a concentration of strain at the Yehudi break. The idealization of the structure used in the FEM is not very effective at capturing the large variations in strain that occur locally to the Yehudi break. The FEM was designed to capture the overall mode shapes, not the local strains in this region. Therefore, the FEM-based model is not as accurate at this point, but still is effective at representing the strains. Also, there is some spanwise waviness in the static loading ground test data that is not captured by the FEM-based FOSS model. The FEM is not an exact representation of the structure, so some local variations are expected. The waviness has also been observed as an artifact of the FOSS sensing system. These variations may limit the ability to capture high order modes.

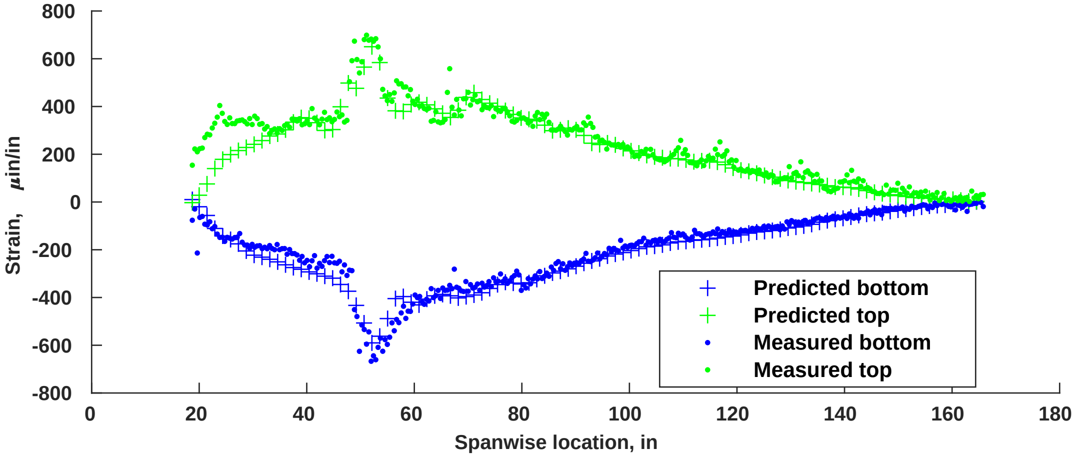

a) Left wing, up bending, load case 12.

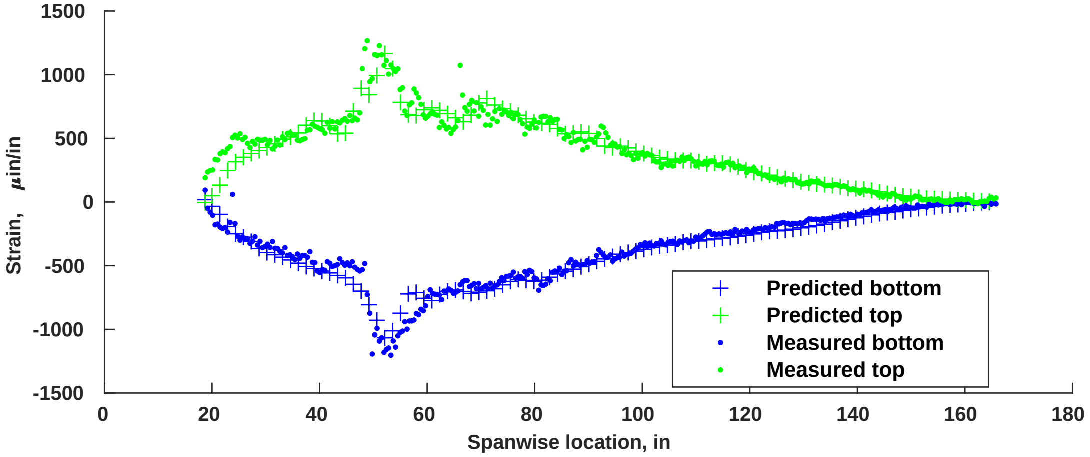

b) Right wing, up bending, proof case.

Fig. 14 Strain on trailing edge fiber measured on X-56A wing during static loading and from FEM-based FOSS model.

The final segment of the fiber considered is the mid chord run inboard of the Yehudi break shown in Fig. 15. The midspan fiber run overall matches well to the static loading ground-test data. There is a peak in the strains in the top fiber closer to the Yehudi break that is not captured in the FEM-based model.

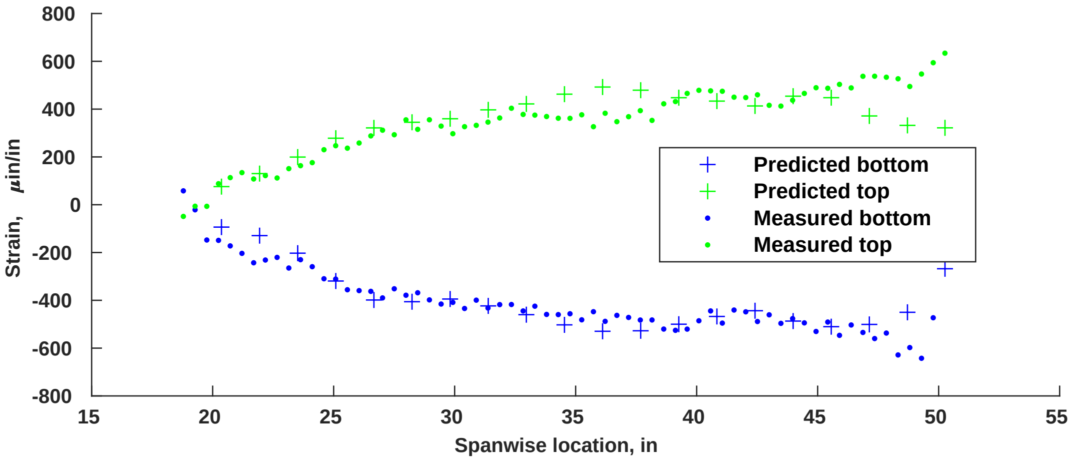

a) Left wing, up bending, load case 12**.**

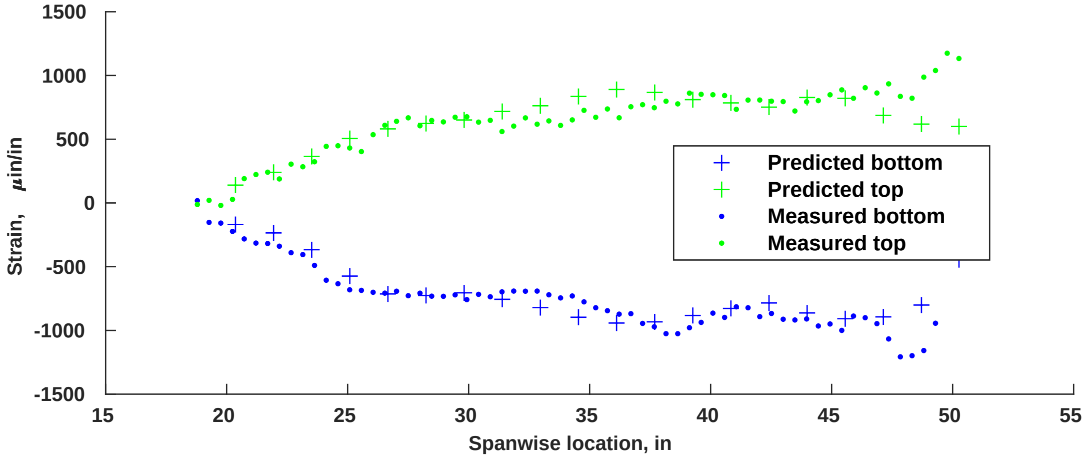

b) Right wing, up bending, proof case.

Fig. 15 Strain on Yehudi fiber measured on X-56A wing during static loading and from FEM-based FOSS model.

1. Characterization of Noise

Because the FOSS system uses light waves to interrogate the gratings, there is an alternating nature to the excitation. In contrast, traditional foil gauges typically use a steady voltage for excitation. The dynamic nature of the excitation and the significant signal processing required to convert the data to engineering units, means that the FOSS has very complex noise characteristics. Because of this signal processing, the noise is colored which means that there is some underlying statistical process, and the noise at each time is not independent. Because the static loading ground tests are steady, it was used to better understand the nature of the noise in FOSS.

The effect of these sensor dynamics on the noise are characterized by the autocorrelation and partial autocorrelation function in Fig. 16. These autocorrelation functions show the strength of the linear relationship between the current and previous, i.e., lagged, values. The autocorrelation function is also equal to the inverse Fourier transform of the power spectral density. The autocorrelation function, Figs. 16a and 16b, does offer insights to the underlying differential equations that can be difficult to see in a power spectral density [12]. The gradual decay of the autocorrelation function indicates that there is a strong 1st order relationship in the noise. This relationship is further clarified by the partial autocorrelation function. The value of the partial autocorrelation is a good estimate of the coefficient of the discrete time transfer function of the measurement noise process. The partial autocorrelation, Figs. 16c and 16d, shows that there are higher order dynamics as well. The smaller peaks at lags 19 and 20 indicate that there is a periodic behavior to the noise. However, without further understanding of the nature of the FOSS system it is difficult to understand what is causing this.

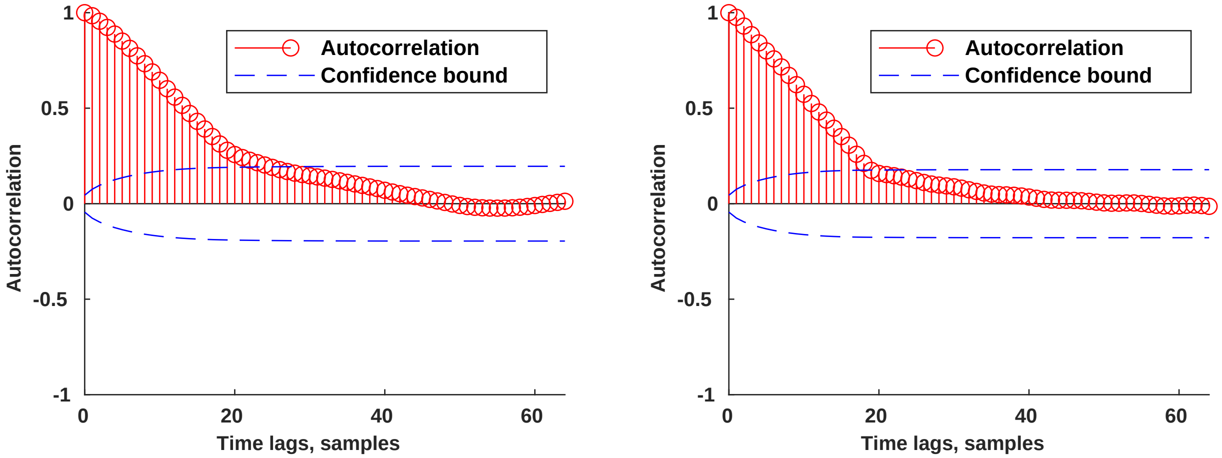

a) Autocorrelation of left wing, up bending, load case 12.

b) Autocorrelation of right wing, up bending, proof load.

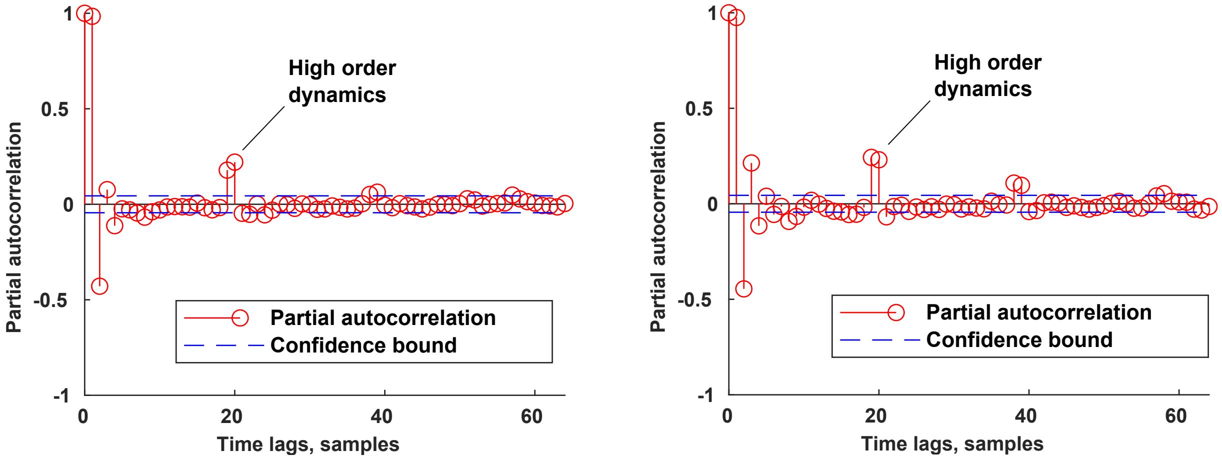

c) Partial autocorrelation of left wing, up bending, load case 12.

d) Partial autocorrelation of right wing, up bending, proof load.

Fig. 16 Time autocorrelation of FOSS noise.

In addition to the time autocorrelation, we can look at spatial autocorrelation of the noise at a grating to its neighbors. The spatial autocorrelation is shown in Fig. 17. The spatial autocorrelation does cutoff very quickly for adjacent gratings. However, it is still above the uncertainty threshold. These results indicate that there is a weak relationship in the noise between the adjacent gratings. The spatial correlation can be seen as the waviness observed in Fig. 14.

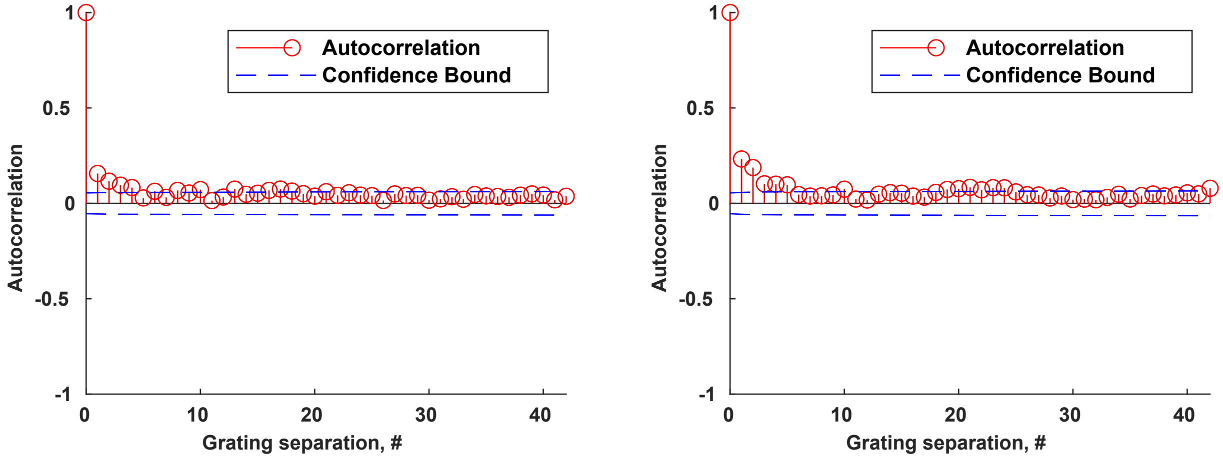

a) Autocorrelation of left wing, up bending, load case 12.

b) Autocorrelation of right wing, up bending, proof load.

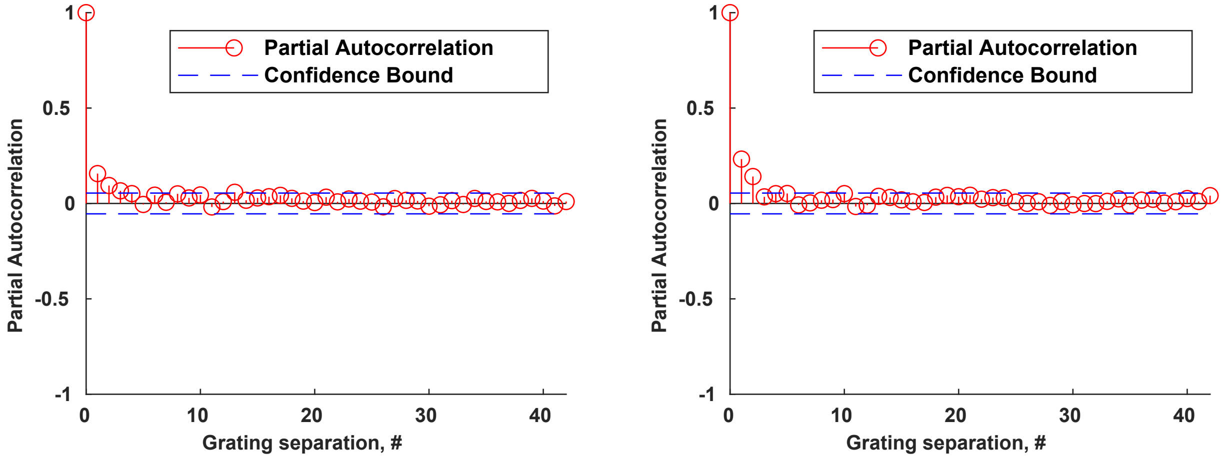

c) Partial autocorrelation of left wing, up bending, load case 12.

d) Partial autocorrelation of right wing, up bending, proof load.

Fig. 17 Spatial autocorrelation of FOSS noise.

Although the previous analysis showed that the adjacent fibers do not affect their neighbors, when we look at the correlation matrix of all of the gratings in Fig. 18 we see that several gratings are strongly correlated to each other. The correlation of Fig. 18 would appear to contradict the previous analysis. Unlike a true spatial effect, these correlations are spurious and completely random.

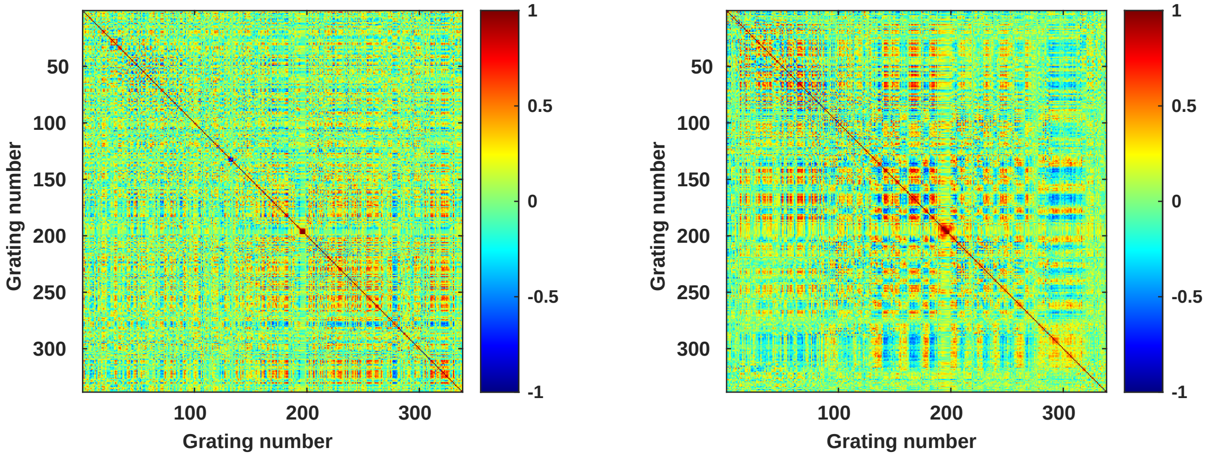

a) Left wing, up bending, load case 12. **b) Right wing, up bending, proof load.**

Fig. 18 Correlation matrix of FOSS noise.

The correlations are occurring because of the time correlations, rather than some spatial effect. Because all the gratings have a similar dynamic process that colors the noise, it is inevitable that some gratings will be well synchronized due to a random phasing. They cannot be predicted, and the pattern of correlations will change between tests. The correlation implies that there will be "noise" modes present in any test data. However, we cannot predict these a priori, and must be calculated from the current data set.

V. Conclusion

A FEM-based model of the FOSS was generated using FEM strains from shell elements that are translated to output strains. The FEM-based FOSS modeling was validated using static loading ground-test data from the X-56A aircraft and a set of correction factors were defined to improve the correlations. The static loading ground-test data was also used to help characterize the unique noise characteristics of the advance sensing system like FOSS. However, it does exhibit significant correlations in time and along the fiber that could complicate analyses with the sensor.

VI. Acknowledgments

This work has been supported by the NASA Space Technology Mission Directorate Center Innovation Fund, the NASA Advanced Air Transport Technology Program, and the NASA Flight Demonstrations and Capabilities Project.

References

[1] Noll, T. E., Brown, J. M., Perez-Davis, M. E., Ishmael, S. D., Tiffany, G. C., and Gaier, M., "Investigation of the Helios Prototype Aircraft Mishap, Vol. 1 - Mishap Report," NASA, 2004.

[2] Livne, E., "Aircraft active flutter suppression: State of the art and technology maturation needs," *Journal of Aircraft*, Vol. 55, No. 1, 2018, pp. 410–452.
https://doi.org/10.2514/1.C034442.

[3] Chan, P. H. M., "Fiber Optics Sensing System (FOSS) at NASA Armstrong Flight Research Center (AFRC): Summary and Recent Deployments," *Edwards Technical Symposium*, 2018.

[4] Ko, W. L., and Fleischer, V. T., "Further Development of Ko Displacement Theory for Deformed Shape Predictions of Nonuniform Aerospace Structures," NASA TP-2009-214643, 2009.

[5] Pak, C.-g., "Wing Shape Sensing from Measured Strain," *AIAA Journal*, Vol. 54, No. 3, 2016, pp. 1068–1077.
https://doi.org/10.2514/1.J053986.

[6] Suh, P. M., Chin, A. W., and Mavris, D. N., “Virtual Deformation Control of the X-56A Model with Simulated Fiber Optic Sensors,” AIAA 2013-4844, Boston, MA, Aug. 2013.
https://doi.org/10.2514/6.2013-4844.

[7] Poole, D., *Linear Algebra: A Modern Introduction*, Thompson Brooks/Cole, Toronto, 1996.

[8] Shames, I. H., and Dym, C. L., *Energy and Finite Element Methods in Structural Mechanics*, Taylor & Francis Books, Inc., Great Britain, 2003.

[9] Beranek, J., Nicolai, L., Buonanno, M., Burnett, E., Atkinson, C., Holm-Hansen, B., and Flick, P., “Conceptual Design of a Multi-Utility Aeroelastic Demonstrator,” AIAA 2010-9350, Sep. 2010.
https://doi.org/10.2514/6.2010-9350.

[10] Chin, A. W., Truong, S. S., and Spivey, N. D., “X-56A Structural Dynamics Ground Testing Overview and Lessons Learned,” AIAA 2020-1015, Orlando, FL, Jan. 2020.
https://doi.org/10.2514/6.2020-1015.

[11] Ouellette, J. A., Boucher, M. J., and Suh, P., “Using Distributed Fiber-optic Strain Sensing to Estimate Generalized Modal Coordinates from Flight-test Data,” AIAA 2023–2069, National Harbor, MD, Jan. 2023.
https://doi.org/10.2514/6.2023-2069.

[12] Box, G. P., and Jenkins, G. M., *Time Series Analysis: Forecasting and Control*, Holden-Day Inc., 1976.